

# Enhanced inner core fine-scale heterogeneity towards Earth's centre

<https://doi.org/10.1038/s41586-023-06213-2>

Received: 9 July 2022

Accepted: 12 May 2023

Published online: 5 July 2023

 Check for updates

Guanning Pang<sup>1,5</sup>✉, Keith D. Koper<sup>1</sup>, Sin-Mei Wu<sup>1,6</sup>, Wei Wang<sup>2,7</sup>, Marine Lasbleis<sup>3,8</sup> & Garrett Euler<sup>4</sup>

Earth's inner core acquires texture as it solidifies within the fluid outer core. The size, shape and orientation of the mostly iron grains making up the texture record the growth of the inner core and may evolve over geologic time in response to geodynamical forces and torques<sup>1</sup>. Seismic waves from earthquakes can be used to image the texture, or fabric, of the inner core and gain insight into the history and evolution of Earth's core<sup>2–6</sup>. Here, we observe and model seismic energy backscattered from the fine-scale (less than 10 km) heterogeneities<sup>7</sup> that constitute inner core fabric at larger scales. We use a novel dataset created from a global array of small-aperture seismic arrays—designed to detect tiny signals from underground nuclear explosions—to create a three-dimensional model of inner core fine-scale heterogeneity. Our model shows that inner core scattering is ubiquitous, existing across all sampled longitudes and latitudes, and that it substantially increases in strength 500–800 km beneath the inner core boundary. The enhanced scattering in the deeper inner core is compatible with an era of rapid growth following delayed nucleation.

Earth's solid inner core acquires a texture, or fabric, as the mostly iron grains solidify, lithify and age. The fabric imparts seismic anisotropy through the alignment of intrinsically anisotropic crystal lattices, iron grains with preferred shapes or both<sup>1,2</sup>. Studies of seismic waves transmitted through the inner core (PK<sub>Df</sub>) show a surprising amount of complexity in inner core fabric<sup>3</sup>. The current standard model of the inner core comprises a nearly isotropic outer layer with thickness variations between quasieastern (qEH) and quasiwestern (qWH) hemispheres of approximately 50–200 km underlain by a layer reaching a depth of approximately 600–700 km beneath the inner core boundary (ICB) that has strong cylindrical anisotropy about Earth's rotation axis, surrounding an innermost inner core that has a distinct orientation of anisotropy and is slightly offset from the centre of Earth<sup>4–6</sup>. Continued seismic mapping of inner core fabric is important because the fabric records the history and evolution of Earth's core, which in turn, bear on the history and evolution of Earth's magnetic field, convection in the fluid outer core and heat flow into the base of the mantle.

The fine-scale structure that creates inner core fabric scatters high-frequency seismic waves, creating a long train of coda waves that follow precritical reflections from the ICB (PKiKP), known as inner core scattered (ICS) energy<sup>7</sup> (Fig. 1). The duration, shape and intensity of ICS depend on the properties of the inner core fabric, such as the size, shape, alignment and orientation of the solid iron grains<sup>8,9</sup>. While numerous studies have observed regional variations in the properties of waves transmitted through Earth's inner core<sup>6</sup>, relatively few address regional variation in ICS, which provides a complementary picture of inner core fabric<sup>10–12</sup>. Furthermore, because of the difficulties in observing ICS energy, the geographical sampling in previous inner core

scattering studies has often been spatially limited: for instance, to data from a single seismic array<sup>13</sup> or to localized patches of the inner core<sup>14,15</sup>.

In this study, we use seismograms from 2,455 earthquakes recorded by a global array of 20 small-aperture seismic arrays to observe ICS energy across a nearly complete range of longitudes, at equatorial and midrange latitudes and in both polar regions (Fig. 1). Most of the seismic arrays are part of the International Monitoring System (IMS), which is operated by the Preparatory Commission for the Comprehensive Nuclear-Test-Ban Treaty Organization for the purpose of monitoring the globe for underground nuclear explosions. The arrays consist of high-quality sensors deployed in boreholes for optimal detection of short-period P waves at regional-to-telesismic distances. We supplement the 18 IMS arrays with data from two temporary seismic deployments in Antarctica to enhance coverage in the Southern Hemisphere. The overall geometry provides unprecedented global sampling of ICS energy with corridors of crossing ray paths that promote robust observations. We use a multiple-scattering phonon approach<sup>16</sup> to model the observations and create a series of one-dimensional profiles of scattering strength in the inner core, which are stitched together to create a quasiglobal three-dimensional (3D) map of inner core scattering strength. The new Earth model provides fresh insight into the growth history of the inner core.

## ICS energy observations

We created the ICS dataset using seismograms of moment magnitude ( $M_w$ )  $\geq 5.7$  earthquakes located 50°–75° away from an array. In this distance range, almost all the energy incident on the ICB is transmitted

<sup>1</sup>Department of Geology and Geophysics, University of Utah, Salt Lake City, UT, USA. <sup>2</sup>Department of Earth Sciences, University of Southern California, Los Angeles, CA, USA. <sup>3</sup>Laboratoire de Planétologie et Géosciences, UMR 6112, Université de Nantes, CNRS, Nantes, France. <sup>4</sup>Los Alamos National Laboratory, Los Alamos, NM, USA. <sup>5</sup>Present address: Department of Earth and Atmospheric Sciences, Cornell University, Ithaca, NY, USA. <sup>6</sup>Present address: Swiss Seismological Service, ETH Zurich, Zurich, Switzerland. <sup>7</sup>Present address: Key Laboratory of Earth and Planetary Physics, Institute of Geology and Geophysics, Chinese Academy of Sciences, Beijing, China. <sup>8</sup>Present address: Bureau Veritas Marine & Offshore, Paris La Défense, France. <sup>✉</sup>e-mail: g.Pang@utah.edu

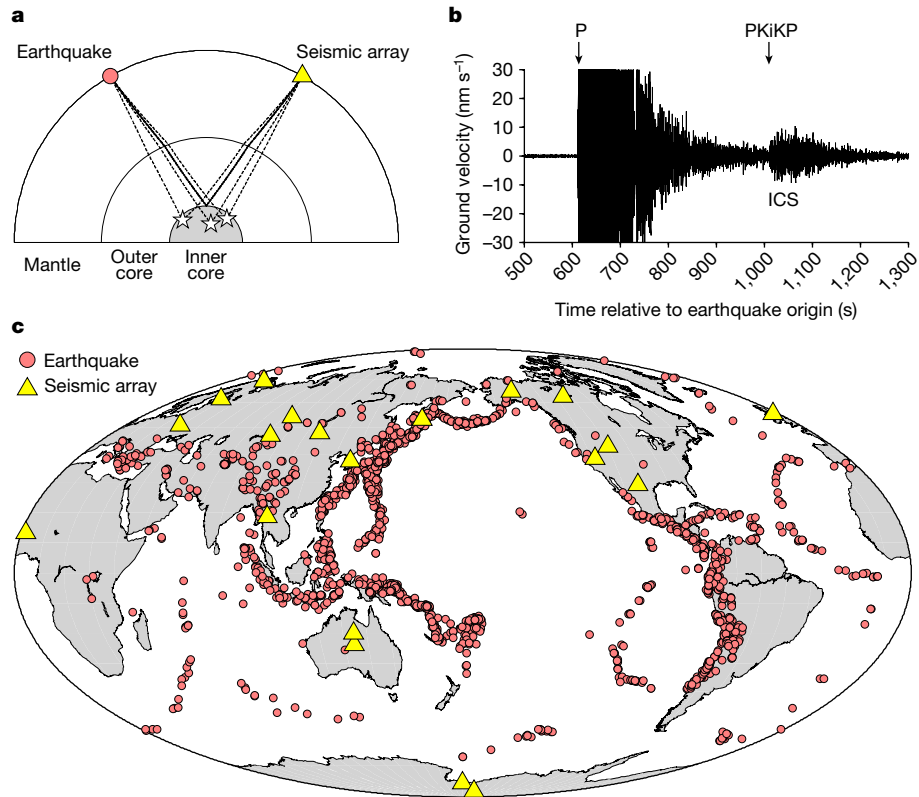


**Fig. 1 | Example of ICS and map of arrays.** **a**, Schematic cross-section illustrating the ray paths of PKiKP (solid lines) and the ICS energy (dashed lines). **b**, Example delay-and-sum beam at the ILAR seismic array in central Alaska. The beam was formed at the PKiKP slowness in a 2- to 4-Hz passband. The earthquake ( $M_w$  6.9, 8 November 2011 02:59:08 coordinated universal time

(UTC), 27.32° N, 125.62° E, 225-km depth, United States Geological Survey–National Earthquake Information Center (USGS–NEIC) occurred northeast of Taiwan, about 64.6° away from ILAR. **c**, Map of seismic arrays and earthquakes used in this study.

across the interface<sup>17</sup>. The amplitude of the reflected PKiKP phase is near zero, and heterogeneity within the body of the inner core is required to generate significant PKiKP coda<sup>15</sup>. The arrays are appropriately sized (9–24 elements with apertures of 2–40 km) (Extended Data Fig. 1 and Extended Data Table 1) to enhance energy at the high frequencies (greater than or equal to 1 Hz) in which ICS is observed. ICS is identified at the arrays by its steep arrival direction, which is similar to the PKiKP direction of arrival. The arrays significantly enhance the signal-to-noise ratio of ICS, allowing it to be observed for hundreds of seconds (Fig. 1b).

Most of the arrays used in this study are part of the IMS, which operates in support of the Commission for the Comprehensive Nuclear-Test-Ban Treaty Organization, and meet rigorous siting and reliability requirements. IMS seismometers are commonly emplaced in boreholes in regions with low cultural noise to enhance the observability of small seismic signals produced by underground nuclear weapons tests. Many of the arrays in our study have not previously been used to study deep Earth structure. Notable examples include PS25 in Songino, Mongolia; PS26 in Torodi, Niger; PS45 in Malin, Ukraine (AKASG) and PS36 in Petropavlovsk-Kamchatskiy, Russia. The broad longitudinal coverage of the IMS arrays is important because of the quasihemispherical dichotomy in inner core structure<sup>18</sup>. To enhance coverage in the Southern Hemisphere, we collected data from two temporary seismometer deployments in Antarctica with small-enough aperture and high-enough station coherence to be used as teleseismic arrays (Fig. 1c).

We followed the framework presented in Wu et al.<sup>15</sup> for identifying and extracting ICS energy (Methods). After beamforming and slowness analysis to identify ICS, we constructed envelopes of the

delay-and-sum PKiKP beams (Fig. 1b and Extended Data Fig. 2), removed the background energy corresponding to the low-slowness component of P + Pcp + PP energy and stacked the denoised ICS envelopes from similar inner core geographic regions to obtain characteristic ICS envelopes (Fig. 2a). Source and receiver effects are mitigated by the beamforming, denoising, normalization and stacking procedures<sup>15</sup>. We find similar envelope shapes for paths that sample the same patch of the inner core with distinct source–receiver combinations (Extended Data Fig. 3), reinforcing the idea that the denoised PKiKP coda envelopes are primarily sensitive to the inner core.

We observe robust ICS envelopes for all 20 geographic regions of the inner core that were well sampled (Extended Data Fig. 4), indicating that fine-scale heterogeneity in the inner core is ubiquitous. The scattered energy initially grows for tens of seconds after the predicted PKiKP arrival before fading back into the background noise over hundreds of seconds, resulting in spindle-shaped envelopes (Fig. 2 and Extended Data Fig. 5). We characterized the envelopes with a growth time ( $t_{\text{growth}}$ ), defined as the time taken from the predicted PKiKP arrival to the maximum amplitude, and a decay time ( $t_{\text{decay}}$ ), defined as the time taken to decay to 1/e (approximately 0.37) of the maximum amplitude (Fig. 2a and Methods). Growth times ranged from 30 to 80 s, and decay times ranged from 60 to 150 s (Fig. 2). The ICS envelopes have total durations of 100–250 s if we define the duration,  $t_{\text{total}}$ , as the sum of  $t_{\text{growth}}$  and  $t_{\text{decay}}$  (Fig. 2). We emphasize that our definition of duration is designed to be independent of the background noise level and so, is necessarily conservative; it is common to observe ICS energy for 25–75 s after  $t_{\text{total}}$  (Fig. 2 and Extended Data Fig. 5).

According to elastic scattering theory, existing models of inner core heterogeneity<sup>7,12,14</sup> have mean free paths longer than 2,000 km;

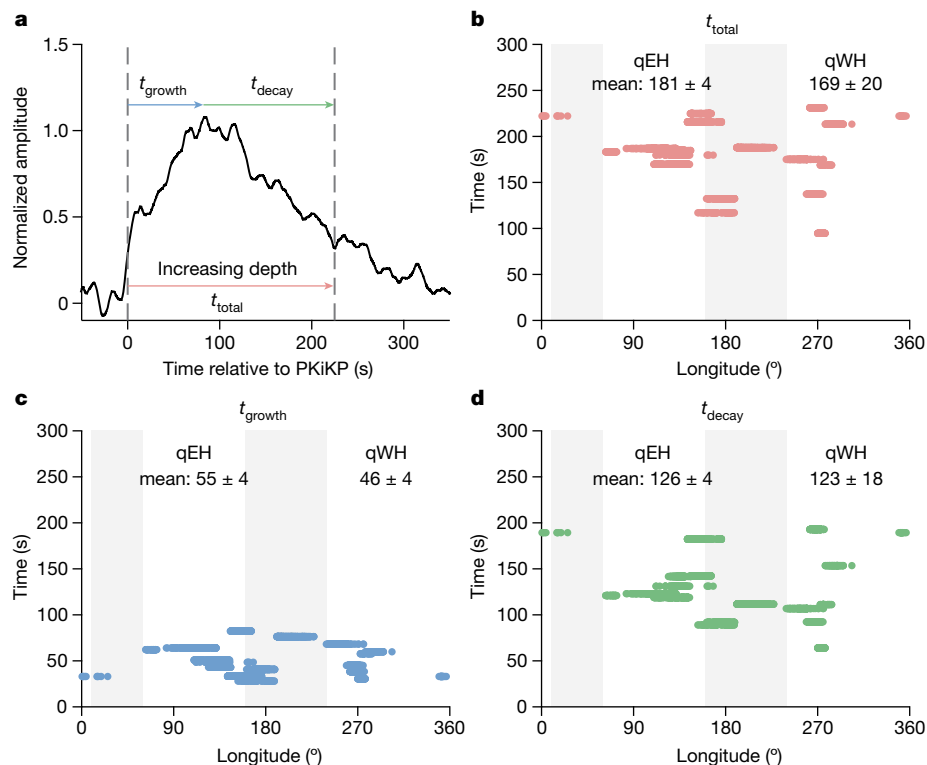


**Fig. 2 | ICS energy characteristics.** **a**, Example of a stacked PKiKP coda envelope from ILAR. The x axis is time relative to the predicted PKiKP arrival time. The coloured arrows indicate the duration ( $t_{\text{total}}$ ), growth ( $t_{\text{growth}}$ ) and decay ( $t_{\text{decay}}$ ) times. **b–d**, These measures are also shown as a function of longitude in **b**, **c** and **d**, respectively. The grey areas illustrate the variation in published hemispherical

boundaries, which range from 10° E to 60° E and 160° E to 240° E beneath Africa and the Pacific Ocean, respectively<sup>15,19</sup>. The mean and the standard error are reported for qEH and qWH, which are based on the measurements sampling 60° E to 160° E for the qEH and greater than or equal to 240° E for qWH.

therefore, single scattering is a good approximation, and the extraordinarily long ICS durations cannot be explained by a thin, crust-like scattering layer just beneath the ICB. The long ICS durations require that heterogeneity exists deep within the inner core. Because of the relatively high attenuation in the inner core, the scattering deep within the inner core is likely stronger than that near the ICB such that substantial ICS energy can be recorded at the surface. There is weak evidence for the qWH (greater than or equal to 240° E) having shorter-duration ICS than the qEH (60° E to 160° E) (Fig. 2); however, a Student's *t* test shows no significant difference in the means of  $t_{\text{growth}}$ ,  $t_{\text{decay}}$  and  $t_{\text{total}}$  between the two hemispheres. The intrahemispherical variations in duration are comparable with the interhemispherical variations (Fig. 2 and Extended Data Fig. 5). It is also possible that geographical averaging, owing to the broad Fresnel-like sensitivity zones of hundreds of kilometres for the coda energy, would obscure a sharp boundary in our dataset if such a boundary exists in Earth<sup>15,19</sup>.

## Models of inner core heterogeneity

We modelled the ICS observations using a multiple-scattering phonon technique<sup>16</sup> that simulates PKiKP coda envelopes for stochastically defined distributions of inner core heterogeneity (Methods). This approach parametrizes the scattering medium using an autocorrelation function with two free parameters—the root-mean-square (RMS) variation from a reference velocity model and the spatial correlation length. These two parameters jointly determine the elastic diffusivity,  $D$ , which is the key parameter for quantifying the scattering strength of a heterogeneous medium<sup>20,21</sup> (Methods and Extended Data Fig. 6). Based on elastic scattering theory, the level of backscattered energy is typically proportional to  $D^{-1.5}$ , such that smaller  $D$  means stronger

backscattering<sup>21</sup>. We generated a suite of 79 Earth models characterized by different diffusivities in up to three distinct inner core layers using AK135 (ref. 22) as the reference velocity model. Our simulations account for mantle scattering as well as inner core scattering, and we used the same denoising, stacking and normalization procedure on the synthetic coda envelopes as we used with the data.

We searched for the best-fitting inner core scattering model for each observed ICS envelope stack using a modified L2 norm that explicitly accounts for the growth and decay rates of the ICS envelope (Extended Data Fig. 7). We combined the elastic wave diffusivities in the uppermost 800 km of the inner core from the 20 best-fitting one-dimensional scattering models (Extended Data Fig. 5) into a 3D map of inner core heterogeneity using  $D^{-1.5}$  as a proxy of scattering strength (Fig. 3). Our results indicate that fine-scale heterogeneity exists globally to depths of 500–800 km beneath the ICB (Fig. 3). Because of anelastic attenuation, we lose resolution at greater depths. The scattering strength in the uppermost 150 km of the inner core exhibits substantial lateral variations with relatively strong scattering beneath southeastern Asia, northern Latin America and south of New Zealand (Fig. 3a). There is also strong scattering beneath the northeast of Eurasia, which is consistent with recent regional mapping of inner core fine-scale heterogeneity<sup>13</sup>. The strong scattering beneath southeastern Asia is consistent with predictions of fast inner core growth in the past 100–300 Myr beneath the region<sup>23</sup>. Scattering strength 150–500 km below the ICB shows similar lateral variations with increasing scattering strength beneath the Gulf of Alaska and Atlantic Ocean (Fig. 3b,c). The regions with strong scattering spread from the centre of the qEH to the central qWH (Fig. 3), and there is only marginal evidence for a hemispherical dichotomy in scattering strength. Student's *t* tests show no significant difference in the means of  $D^{-1.5}$  between hemispheres, consistent with

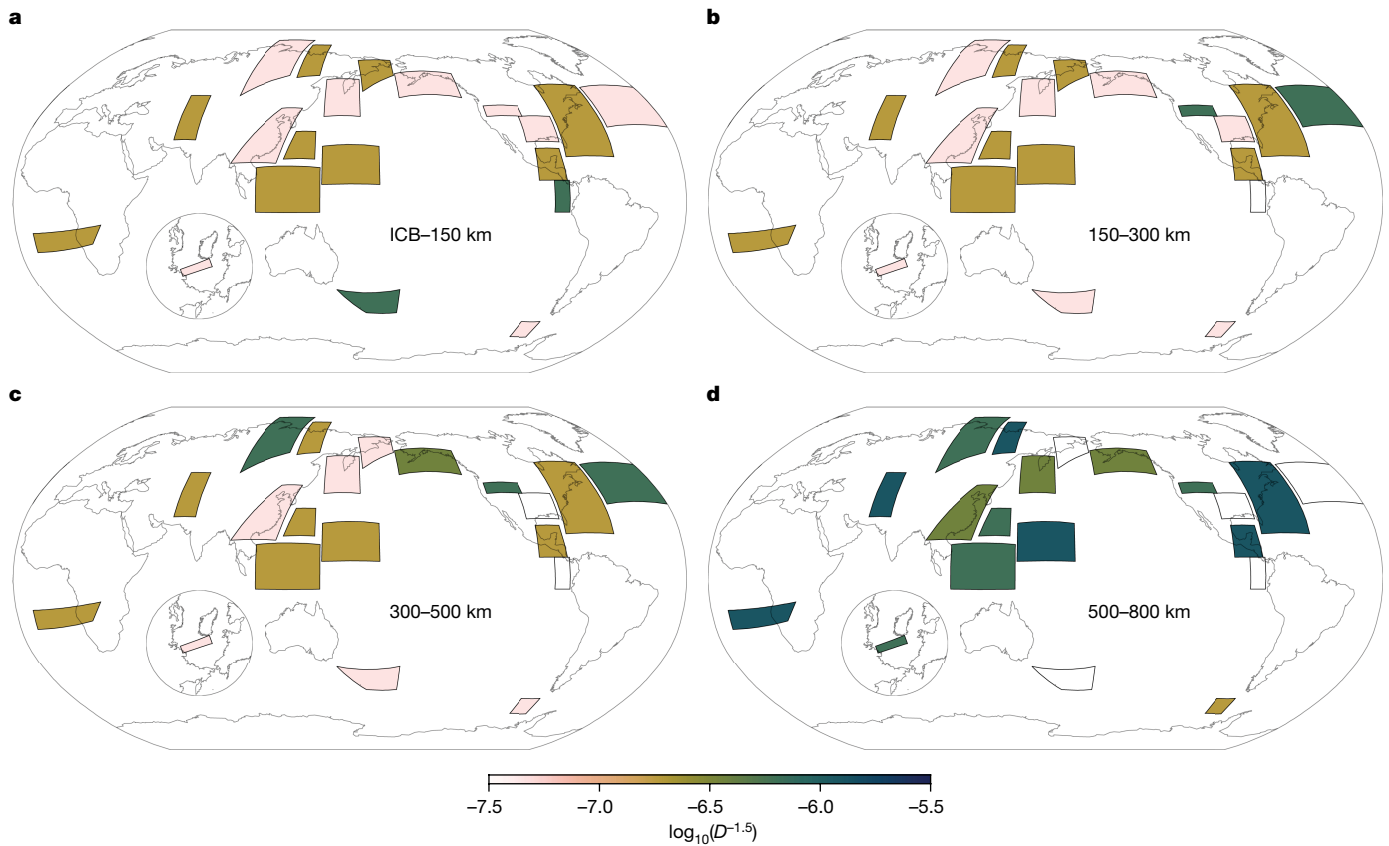


**Fig. 3 | Inner core 3D scattering structure.** a–d, Backscattering strength in the uppermost 150-km inner core (a), 150–300 km beneath the ICB (b), 300–500 km below the ICB (c) and 500–800 km below the ICB (d). The scattering

strength is represented by  $D^{-1.5}$ , where  $D$  is the seismic diffusivity. Larger values of  $D^{-1.5}$  mean stronger backscattered energy.

what we observed in the raw data that evidence for sharp hemispherical boundaries is insignificant (Fig. 2).

The scattering strength 500–800 km below the ICB is stronger than that in the uppermost 500 km but with weaker lateral variations (Fig. 3d). For 16 of the 20 well-sampled regions of the inner core, increasing heterogeneity strength with depth is required to match the observations. There are some small underpredictions of late coda energy for many ICS envelopes, suggesting that our models may underestimate the deeper scattering. The average elastic diffusivity ( $D$ ) is approximately  $1.4 \times 10^4 \text{ m}^2 \text{ s}^{-1}$  at 700 km below the ICB, only about one third of the average value of approximately  $4.9 \times 10^4 \text{ m}^2 \text{ s}^{-1}$  at 200 km below the ICB. The average scattering strength ( $D^{-1.5}$ ) 700 km below the ICB is about six times larger than the average scattering strength 200 km below the ICB (Fig. 4a). It is well known that coda decay rates depend on anelastic attenuation<sup>24</sup>; therefore, we experimented with increasing intrinsic attenuation ( $Q_i$ ) from the AK135 value of 360 to 600, which is the maximum value observed in regional studies of transmitted waves. Our modelling results remained similar in the sense that stronger heterogeneity deeper in the inner core was required to match the observations. While the stronger heterogeneity deeper in the inner core is required, the sharpness of the increase is less well resolved. Smoother models involving a strong radial gradient in scattering strength cannot be excluded.

The enhanced heterogeneity can arise from changes in the size, shape, alignment or orientation of the iron grains and suggests a distinct texture within the deeper inner core<sup>2,8,9</sup>. Previous studies have proposed the existence of a distinct innermost inner core based on a change in the orientation of seismic anisotropy in transmitted waves<sup>25,26</sup>. Our observation of increased scattering 500–800 km beneath the

ICB is consistent with the most recent transmitted wave study, which used a regularization-free global search methodology to estimate a depth of approximately 570 km beneath the ICB for the boundary of the innermost inner core<sup>27</sup>. This consistency suggests that changes in the shape, orientation or size of iron grains<sup>9</sup>, rather than a change in lattice-preferred orientation of iron crystals, may be responsible for radial variations of anisotropy within the inner core.

### Inner core nucleation and growth

Solidification texturing is the most likely micromechanism for generating fine-scale heterogeneity in the inner core. The alternative interpretation, deformational texturing, is likely too slow<sup>28</sup> to generate abrupt changes in seismic heterogeneity. The lateral variations of seismic heterogeneity in the uppermost 150 km of the inner core are likely imprinted by mantle-induced lateral variations in the inner core growth rate in the past 100–300 Myr (ref. 23). The deeper inner core exhibits a fossil texture<sup>29</sup> such that the heterogeneity structure in the deeper inner core records the history of inner core growth. The significantly enhanced fine-scale heterogeneity we observe in the deeper inner core can be interpreted as evidence for an abrupt change in the growth history of the inner core<sup>30–32</sup>.

A plausible scenario for two-stage inner core growth involves supercooling of the primordial fluid core such that inner core formation is delayed until the nucleation barrier is overcome<sup>30,31</sup>. After surpassing the nucleation barrier, the inner core would initially grow very rapidly before transitioning to a steady growth regime<sup>30</sup> (Extended Data Fig. 8). The delayed nucleation would increase the porosity in the central part of the inner core<sup>33</sup>, changing the volume fraction of trapped fluid and

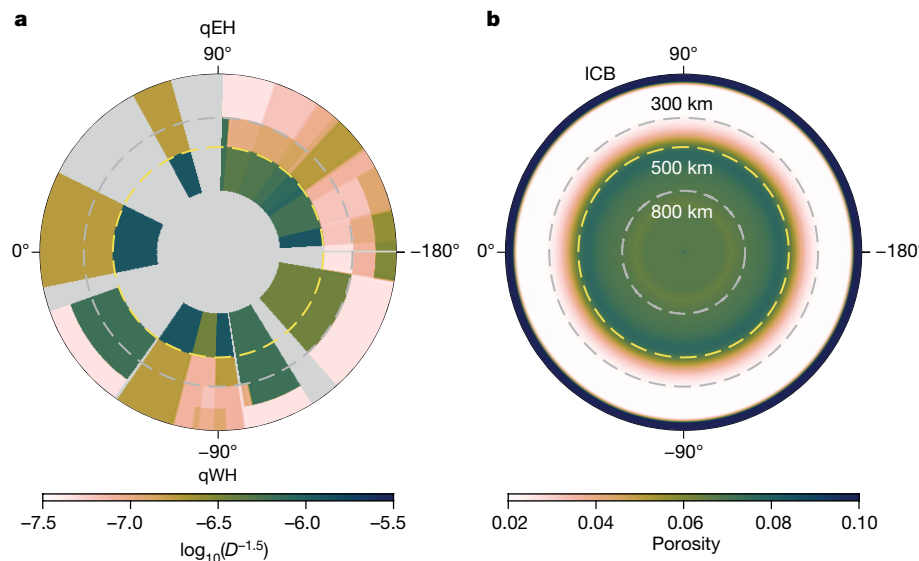


**Fig. 4 | Variation of scattering strength and porosity in the equatorial plane viewed from Earth's pole.** **a**, Global scattering variation along the inner core radius on the equatorial plane. The depths below ICB are marked as dashed circles and are labelled in **b**. The scattering strength is averaged over latitude. The grey patches indicate unconstrained portions of the inner core, either no

data (patches along azimuths) or scattering is not required (patches inside inner core). **b**, Inner core porosity structure for an inner core growth model with nucleation delayed until  $0.07 \tau_{ic}$ . Yellow lines mark a depth of 500 km below ICB, where the scattering strength increases towards the deep inner core observed globally.

light elements. The trapped fluid would freeze later in time, presumably leading to a distinct texture compared with the upper part of the inner core<sup>32</sup>, which might in principle be observed in ICS energy. We can narrow the timing of inner core nucleation by comparing our radial heterogeneity profile with the evolution of inner core porosity structure based on a simplified two-phase system driven by the density difference between liquid and solid<sup>33</sup>. Applying this model (Methods), the increase in heterogeneity 500–800 km below the ICB suggests that the timing of the delayed nucleation is approximately  $0.07$ – $0.12 \tau_{ic}$ , where  $\tau_{ic}$  is the presumed inner core age in the canonical growth model, which ignores the nucleation barrier<sup>34</sup> (Fig. 4 and Extended Data Fig. 9). The corresponding initial inner core radius at the end of the fast-growth stage is between  $0.35$  and  $0.43 R_{ICB}$ , corresponding to a supercooling temperature of  $20$ – $33$  K during inner core nucleation<sup>30</sup> (Extended Data Fig. 8).

## Online content

Any methods, additional references, Nature Portfolio reporting summaries, source data, extended data, supplementary information, acknowledgements, peer review information; details of author contributions and competing interests; and statements of data and code availability are available at <https://doi.org/10.1038/s41586-023-06213-2>.

1. Deguen, R. Structure and dynamics of Earth's inner core. *Earth Planet. Sci. Lett.* **333**, 211–225 (2012).
2. Cormier, V. F. Texture of the uppermost inner core from forward-and back-scattered seismic waves. *Earth Planet. Sci. Lett.* **258**, 442–453 (2007).
3. Sun, X. & Song, X. Tomographic inversion for three-dimensional anisotropy of Earth's inner core. *Phys. Earth Planet. Inter.* **167**, 53–70 (2008).
4. Deuss, A. Heterogeneity and anisotropy of Earth's inner core. *Annu. Rev. Earth Planet. Sci.* **42**, 103–126 (2014).
5. Souriau, A. & Calvet, M. *Treatise on Geophysics* 2nd edn, Vol. 1 (ed. Schubert, G.) Ch. 1.23 (Elsevier, 2015).
6. Tkalčić, H. Complex inner core of the Earth: the last frontier of global seismology. *Rev. Geophys.* **53**, 59–94 (2015).
7. Vidale, J. E. & Earle, P. S. Fine-scale heterogeneity in the Earth's inner core. *Nature* **404**, 273–275 (2000).
8. Monnereau, M., Calvet, M., Margerin, L. & Souriau, A. Lopsided growth of Earth's inner core. *Science* **328**, 1014–1017 (2010).
9. Calvet, M. & Margerin, L. Shape preferred orientation of iron grains compatible with Earth's uppermost inner core hemisphericity. *Earth Planet. Sci. Lett.* **481**, 395–403 (2018).
10. Koper, K. D., Franks, J. M. & Dombrovskaya, M. Evidence for small-scale heterogeneity in Earth's inner core from a global study of PKiKP coda waves. *Earth Planet. Sci. Lett.* **228**, 227–241 (2004).
11. Leyton, F. & Koper, K. D. Using PKiKP coda to determine inner core structure. 2. Determination of  $Q_c$ . *J. Geophys. Res. Solid Earth* **112**, B05317 (2007).
12. Peng, Z., Koper, K. D., Vidale, J. E., Leyton, F. & Shearer, P. Inner-core fine-scale structure from scattered waves recorded by LASA. *J. Geophys. Res. Solid Earth* **113**, B09312 (2008).
13. Wang, W. & Vidale, J. E. An initial map of fine-scale heterogeneity in the Earth's inner core. *Nat. Geosci.* **15**, 240–244 (2022).
14. Wu, W. & Irving, J. C. Using PKiKP coda to study heterogeneity in the top layer of the inner core's western hemisphere. *Geophys. J. Int.* **209**, 672–687 (2017).
15. Wu, S. M., Pang, G., Koper, K. D. & Euler, G. A search for large-scale variations in the fine-scale structure of Earth's inner core. *J. Geophys. Res. Solid Earth* **127**, e2022JB024420 (2022).
16. Shearer, P. M. & Earle, P. S. The global short-period wavefield modelled with a Monte Carlo seismic phonon method. *Geophys. J. Int.* **158**, 1103–1117 (2004).
17. Souriau, A. & Souriau, M. Ellipticity and density at the inner core boundary from subcritical PKiKP and Pcp data. *Geophys. J. Int.* **98**, 39–54 (1989).
18. Tanaka, S. & Hamaguchi, H. Degree one heterogeneity and hemispherical variation of anisotropy in the inner core from PKP (BC)-PKP (DF) times. *J. Geophys. Res. Solid Earth* **102**, 2925–2938 (1997).
19. Irving, J. C. E. Imaging the inner core under Africa and Europe. *Phys. Earth Planet. Inter.* **254**, 12–24 (2016).
20. Przybilla, J., Wegler, U. & Korn, M. Estimation of crustal scattering parameters with elastic radiative transfer theory. *Geophys. J. Int.* **178**, 1105–1111 (2009).
21. Sato, H., Fehler, M. C. & Maeda, T. *Seismic Wave Propagation and Scattering in the Heterogeneous Earth*. Vol. **496**, (Springer, 2012).
22. Kennett, B. L., Engdahl, E. R. & Buland, R. Constraints on seismic velocities in the Earth from traveltimes. *Geophys. J. Int.* **122**, 108–124 (1995).
23. Aubert, J., Amit, H., Hulot, G. & Olson, P. Thermochemical flows couple the Earth's inner core growth to mantle heterogeneity. *Nature* **454**, 758–761 (2008).
24. Mayeda, K. & Walter, W. R. Moment, energy, stress drop, and source spectra of western United States earthquakes from regional coda envelopes. *J. Geophys. Res. Solid Earth* **101**, 11195–11208 (1996).
25. Beghein, C. & Trampert, J. Robust normal mode constraints on inner-core anisotropy from model space search. *Science* **299**, 552–555 (2003).
26. Ishii, M. & Dziewoński, A. M. The innermost inner core of the earth: evidence for a change in anisotropic behavior at the radius of about 300 km. *Proc. Natl Acad. Sci. USA* **99**, 14026–14030 (2002).
27. Stephenson, J., Tkalčić, H. & Sambridge, M. Evidence for the innermost inner core: robust parameter search for radially varying anisotropy using the Neighbourhood Algorithm. *J. Geophys. Res. Solid Earth* **126**, e2020JB020545 (2021).
28. Yoshida, S., Sumita, I. & Kumazawa, M. Growth model of the inner core coupled with the outer core dynamics and the resulting elastic anisotropy. *J. Geophys. Res. Solid Earth* **101**, 28085–28103 (1996).
29. Deguen, R. & Cardin, P. Tectonic history of the Earth's inner core preserved in its seismic structure. *Nat. Geosci.* **2**, 419–422 (2009).
30. Huguet, L., Van Orman, J. A., Hauck, S. A. II & Willard, M. A. Earth's inner core nucleation paradox. *Earth Planet. Sci. Lett.* **487**, 9–20 (2018).

31. Davies, C. J., Pozzo, M. & Alfè, D. Assessing the inner core nucleation paradox with atomic-scale simulations. *Earth Planet. Sci. Lett.* **507**, 1–9 (2019).
32. Sun, Y., Zhang, F., Mendelev, M. I., Wentzcovitch, R. M. & Ho, K. M. Two-step nucleation of the Earth's inner core. *Proc. Natl Acad. Sci. USA* **119**, e2113059119 (2022).
33. Lasbleis, M., Kervazo, M. & Choblet, G. The fate of liquids trapped during the Earth's inner core growth. *Geophys. Res. Lett.* **47**, e2019GL085654 (2020).
34. Labrosse, S. Thermal evolution of the core with a high thermal conductivity. *Phys. Earth Planet. Inter.* **247**, 36–55 (2015).

**Publisher's note** Springer Nature remains neutral with regard to jurisdictional claims in published maps and institutional affiliations.

Springer Nature or its licensor (e.g. a society or other partner) holds exclusive rights to this article under a publishing agreement with the author(s) or other rightsholder(s); author self-archiving of the accepted manuscript version of this article is solely governed by the terms of such publishing agreement and applicable law.

© The Author(s), under exclusive licence to Springer Nature Limited 2023

# Article

## Methods

### Observing ICS energy

We used 18 IMS small-aperture arrays designed for global monitoring of underground nuclear explosions and two arrays configured from temporary seismic deployments in Antarctica to create the ICS dataset. One Antarctica array (YDW) was subdivided into two subarrays (Extended Data Fig. 1 and Extended Data Table 1). We searched the Global Centroid Moment Tensor ([www.globalcmt.org](http://www.globalcmt.org)) catalogue<sup>35</sup> for earthquakes greater than or equal to  $M_w$  of 5.7 at distances of 50°–75° from an array during 1996–2019. Data from IMS arrays ASAR, ILAR, NVAR, PDAR, TXAR, YKA, WRA and the two Antarctica arrays were available from Incorporated Research Institutions for Seismology ([www.iris.edu](http://www.iris.edu)) as far back as the late 1990s. Data from the 11 remaining IMS arrays were made available for 2013–2018. We ultimately selected viable data from 6,743 distinct earthquake–array combinations for analysis.

Following the approach described in Wu et al.<sup>15</sup>, we applied two array processing techniques to identify ICS energy. Both techniques are available as part of the gPar software package (<https://zenodo.org/record/6784342>). We used delay-and-sum beamforming at the PKiKP slowness predicted by AK135 (ref. 22) and a sliding window beam stacking analysis to enhance the signal-to-noise ratio and identify ICS energy. For most arrays, we filtered the waveforms in a frequency band of 1–2 Hz; however, we filtered data from arrays ARCES, FINES and EKA at 2–4 Hz because of their relatively smaller aperture and denser sensor configuration (Extended Data Fig. 1). In the sliding window analysis, we used a 2-s-long window shifted in 1-s increments. For each time window, we searched over horizontal slowness,  $s_x$  and  $s_y$ , with bounds of plus or minus 15 s per 1° and increments of 0.1 s per 1°, resulting in a  $301 \times 301$  grid. We identified the slowness vector that gave the highest beam power as defined by the RMS amplitude over the time window. Then, we refined the slowness grid to plus or minus 0.1 s per 1° around the optimal slowness and reduced the search increment to 0.00067 s per 1° (resulting in a new  $301 \times 301$  grid) to obtain the final slowness estimate. We computed the waveform coherence by stacking the instantaneous phase of traces shifted according to the final slowness (Extended Data Fig. 2).

After considering the information from sliding window slowness analysis and time-domain beamforming, we classified the data into four categories of ICS observability: (1) conclusive, (2) subtly observed, (3) not clearly observed and (4) corrupt (Extended Data Fig. 2). Category 1 data have the most obvious ICS observations with clear spindle-shaped PKiKP coda energy that is well above the background noise and have a slowness similar to PKiKP. Category 2 data have more subtle ICS observations, and category 3 data have no obvious PKiKP coda energy. Data were defined as corrupt (category 4) if they had instrumentation problems or interfering energy from a second earthquake during the relevant time window. We calculated the delay-and-sum beam envelopes,  $d(t)$ , for observations in categories 1–3 for further analyses (Extended Data Table 1) and discarded category 4 data. As shown in a previous study, ICS is observable in category 3 data when beam envelopes from many earthquakes are stacked<sup>15</sup>.

Scattered energy from the crust and mantle is also prominent on the PKiKP envelopes (because of the small apertures of the arrays) and needs to be removed to isolate ICS characteristics. We used two types of windows during the denoising procedure: the ICS window and the fitting window. The ICS window began at the predicted PKiKP arrival time and lasted 200 s. The fitting windows were two 200-s-long windows that immediately preceded and followed the ICS window and were used to characterize the background energy to be stripped out. The window length was selected through a process of trial and error, resulting in a value that works consistently throughout our dataset. We fit a traditional coda model<sup>21</sup> (equation (1)) simultaneously to the two fitting windows to construct the background energy ( $E_c$ ) to be removed from the ICS window. The functional form of the fitted curve is given by

$$E_c(t) = At^{-B}e^{-C}, \quad (1)$$

in which  $t$  is time relative to the PKiKP arrival and  $A$ ,  $B$  and  $C$  are free parameters determined with a least-squares fit in log space. The denoised envelope,  $S(t) = d(t) - E_c(t)$ , characterizes ICS that has been isolated from the background crust and mantle scattered energy (Extended Data Fig. 2).

We stacked the denoised ICS envelopes of categories 1–3 that sample individual geographic regions (Extended Data Fig. 4) to resolve lower-variance ICS envelopes that capture the average inner core scattering properties in each region. Before stacking, we aligned the envelopes at the predicted PKiKP arrival time and normalized the envelopes to remove the effect of earthquake size. Next, we fit the denoised stacked envelope using equation (1) to obtain stable parametric information about the coda shapes. The fitting windows spanned from 10–40 to 120–200 s following the predicted PKiKP arrival, depending on the envelope shape. Finally, we normalized all the stacked ICS shapes to the maximum amplitude of their best-fitting coda models (Fig. 2a and Extended Data Fig. 5). We found negative  $B$  values and positive  $C$  values for all stacked ICS envelopes. The  $C$  values govern the coda decay rate, while the interplay between  $B$  and  $C$  controls the growth rate. We define the growth time ( $t_{\text{growth}}^{\text{obs}}$ ) as the interval between the theoretical PKiKP arrival and the maximum value of model coda shape ( $-B/C$ ). We define the decay time,  $t_{\text{decay}}^{\text{obs}}$ , of the stacked ICS envelopes as the time taken for the energy to decay to  $e^{-1}$  of its maximum amplitude. Total ICS duration is defined as the time from the theoretical PKiKP arrival to the time that the energy decays to  $e^{-1}$  of its maximum amplitude (that is,  $t_{\text{total}} = t_{\text{growth}}^{\text{obs}} + t_{\text{decay}}^{\text{obs}}$ ).

### Sensitivity of ICS energy and sampling of the inner core

We analysed ICS envelopes recorded at arrays AKASG and CMAR that sample the same inner core region (Extended Data Fig. 3) but different crust and mantle regions to explore the sensitivity of ICS energy. We used one category 1 ICS observation at AKASG and a stacked ICS envelope from three category 2 observations at CMAR (Extended Data Fig. 3a). We obtained similar spindle shapes for envelopes recorded at the two arrays, supporting the idea that the shape of the ICS envelope is mostly sensitive to the inner core region near the PKiKP reflection points (Extended Data Fig. 3). Different ICS envelope shapes would be expected if the ICS energy is created by off great circle heterogeneities because such energy would arrive at AKASG and CMAR at different times with different amplitudes.

We further investigated the ICS sensitivity by performing high-resolution slowness analysis. We picked two time windows: a 5-s time window around the direct PKiKP phase and a 5-s window deep in the coda. For each time window, we grid searched the slowness ( $s_x, s_y$ ) from –5 to 5 s per 1° with increments of 0.01 s per 1°. We also performed 50 bootstrap iterations to estimate uncertainties for the optimal slowness vectors. Extended Data Fig. 3e–g shows example results of slowness analysis for an earthquake recorded at YKA in Canada (Fig. 1 and Extended Data Fig. 1). The back azimuth measured for the coda window is similar to that measured for the direct PKiKP phase, supporting the idea that the ICS energy is being created by great circle heterogeneities geographically near PKiKP bounce points. This result is further supported by similar slowness analysis results (not shown) obtained for different earthquake–array combinations, such as CMAR in Thailand, ILAR in Alaska, WRA in Australia and XHDR in Antarctica.

Because the ICS energy is most sensitive to geographical regions near and beneath the PKiKP reflection points, we can stack the ICS observations with similar PKiKP reflection points to obtain high-quality ICS envelopes. We first stack denoised categories 1–3 ICS envelopes recorded at the same array to obtain lower-variance ICS envelopes. We then stack ICS envelopes from different arrays if they are from overlapping PKiKP reflection regions. Some ICS envelopes from a nearby geographic area are also combined if they have similar shapes based

on 500 bootstrap iterations<sup>15</sup>. Ultimately, we obtain high-quality ICS envelopes (Extended Data Fig. 5) for the 20 geographical areas shown at Extended Data Fig. 4.

### Particle-based multiple-scattering modelling

We modelled the ICS energy using a particle-based Monte Carlo approach that sprays millions of seismic phonons from the source, which scatter according to probabilities from random medium theories<sup>16</sup>. Different versions of this approach have been used to model the scattered high-frequency wave field throughout Earth<sup>12,16,20,36–39</sup>. The heterogeneity is modelled as a continuous random medium that is characterized by the autocorrelation function  $\varepsilon^2 R(a)$ , where  $a$  is the correlation length in kilometres and  $\varepsilon$  is the RMS velocity variation. When  $a$  and  $\varepsilon$  are given, the random velocity perturbations are obtained as a convolution,  $M(x_i, y_k) = \text{Ran}(x_i, y_k) \times \varepsilon^2 R(a, x_i, y_k)$ , where  $(x_i, y_k)$  are the grid coordinates and  $\text{Ran}(x_i, y_k)$  is a random matrix. The input parameters,  $a$  and  $\varepsilon$ , determine four scattering coefficients that describe the power of scattered waves per unit volume as a function of the solid scattering angle,  $g_{ij}(\theta, \phi)$ , in which  $i, j$  are types of incoming seismic waves and outgoing scattered waves (P or S wave, respectively) and  $\theta$  and  $\phi$  give the polar and azimuth angles, respectively, of the scattered wave in the spherical coordinate system<sup>21</sup>.

We can determine the transport mean free path for model P and S waves as  $l^P$  and  $l^S$  from the scattering coefficients (equations 10 and 11 in Przybilla et al.<sup>20</sup>) and then compute the elastic wave diffusivity,  $D$ , as<sup>20,21,40</sup>

$$D = 1/(1 + 2\gamma_0^3) \times ((\alpha_0 l^P)/3 + 2\gamma_0^3 (\beta_0 l^S)/3), \quad (2)$$

in which  $\alpha_0$  and  $\beta_0$  are the P wave velocity and S wave velocity, respectively, and  $\gamma_0$  is the ratio of P wave velocity to S wave velocity. Given the energy radiated from the source as  $W$ , the backscattered energy is<sup>21</sup>

$$E^D(r, t) = W(4\pi Dt)^{-1.5} \times \exp(-r^2/(4Dt) - Q_i^{-1}\omega t) \times H(t), \quad (3)$$

in which  $r$  is distance,  $D$  is elastic wave diffusivity,  $Q_i$  is the intrinsic attenuation factor and  $H(t)$  is a Heaviside function. Thus, the simulated envelope is described by the elastic wave diffusivity determined from a given  $(a, \varepsilon)$  pair after many scattering events, and the synthetic envelopes approximate solutions of the diffusion equation (3) (ref. 20). Different  $(a, \varepsilon)$  pairs may correspond to the same  $D$ , resulting in the same simulated envelopes. In other words, there is a trade-off, making it impossible to determine  $a$  and  $\varepsilon$  independently (Extended Data Fig. 6). However, the elastic wave diffusivity ( $D$ ) can be determined uniquely; thus,  $D$  can be used as a proxy of backscattering strength. Based on equation (3), the backscattered energy is proportional to  $D^{-1.5}$ , such that smaller  $D$  means stronger backscattered energy.

### Fitting ICS observations

We evaluated a series of inner core scattering models to determine best-fitting models for each regional ICS envelope stack. Due to the trade-off between  $a$  and  $\varepsilon$ , we fixed  $a$  at 2 km, which seems to correspond to the minimum value of  $\varepsilon$  when  $D$  is constant<sup>7,15</sup> (Extended Data Fig. 6), and varied  $\varepsilon$ . Wu et al.<sup>15</sup> found that radial changes in heterogeneity structure can affect the shapes of ICS envelopes significantly, especially the growth and decay rates. Hence, we explored three classes of radially varying scattering models: (1) uniform diffusivities in a layer with thicknesses of 150, 300 and 800 km in the uppermost inner core; (2) models containing two layers with smaller diffusivities  $D$  (more heterogeneous) in the deeper layer; and (3) models containing two layers with larger  $D$  (more homogeneous) in the deeper layer. The tops of all models are the ICB. Models that do not have heterogeneity all the way up to the ICB produce a delayed onset in PKiKP coda energy, which is inconsistent with observations. Tests (not shown) show that the interfaces need to shift at least 150 km to generate distinctive synthetic

ICS envelope shapes. Larger separation is needed when the interfaces are in the deep inner core due to the high attenuation. Therefore, the interfaces between the two layers are set to 150, 300 and 500 km below the ICB. This parameterization results in 79 unique models of inner core heterogeneity (Extended Data Fig. 7). We did not consider density variations in the inner core because they are not well constrained<sup>7,15</sup>.

Although the PKiKP coda is less influenced by crust and mantle structure, as shown in Extended Data Fig. 3, we still include mantle scattering in our phonon models to mimic propagation in the real Earth as much as possible. This ensures we can apply the same data processing to the synthetics as we do with the observations. We used the same mantle scattering profile in all models;  $\varepsilon = 2\%$  and  $a = 4$  km for the upper 600 km of the mantle and  $\varepsilon = 0.5\%$  and  $a = 8$  km for the rest of mantle, with all density perturbations set to 0.8 of  $\varepsilon^{12}$ . The mantle scattering profile was obtained from global teleseismic P coda fitting<sup>12,16</sup> without considering potential regional variations in fine-scale mantle heterogeneity<sup>41</sup>. Tests with different mantle scattering models (not shown) indicated that the mantle scattering has minor effects on the shape of PKiKP coda, consistent with the observations in Extended Data Fig. 3. We used the same intrinsic attenuation ( $Q_i$ ) structure for all models: 227 in the layer from 0 to 220 km, 1,383 for the layer from 220 km to core–mantle boundary (CMB) and 360 for the inner core<sup>12</sup>. For each model, we calculated synthetic envelopes at distances of 50°–75° with an interval of 0.5°. We applied the same coda stripping procedure to the synthetics that we applied to the observations and then stacked the denoised synthetic envelopes from 50° to 75° to obtain a final stacked envelope. We fit the traditional coda model (equation (1)) to the stacked simulated envelopes and normalized the envelopes to the maximum of the best-fitting coda models, similar to the data processing. As described previously and shown in Fig. 2, the ICS envelope features were described by two parameters: growth time ( $t_{\text{growth}}$ ) and decay time ( $t_{\text{decay}}$ ). Similar to the observations, the  $t_{\text{growth}}$  of the synthetic ICS envelope was obtained as  $t_{\text{growth}}^{\text{syn}} = -B^{\text{syn}}/C^{\text{syn}}$ , and  $t_{\text{decay}}^{\text{syn}}$  is the time taken for the synthetic envelope to decay to  $e^{-1}$  of its maximum amplitude. To evaluate the quality of the fitting, we defined a misfit parameter as

$$\text{misfit} = \sum (x_i^{\text{syn}} - x_i^{\text{obs}})^2 + (\text{abs}(t_{\text{growth}}^{\text{obs}} - t_{\text{growth}}^{\text{syn}}) + \text{abs}(t_{\text{decay}}^{\text{obs}} - t_{\text{decay}}^{\text{syn}}))/10, \quad (4)$$

in which  $\sum (x_i^{\text{syn}} - x_i^{\text{obs}})^2$  represents the data misfit between synthetic and observation in an L2 norm sense,  $\text{abs}(t_{\text{growth}}^{\text{obs}} - t_{\text{growth}}^{\text{syn}})$  is the misfit in growth times between synthetic and observation and  $\text{abs}(t_{\text{decay}}^{\text{obs}} - t_{\text{decay}}^{\text{syn}})$  is the misfit in decay times between synthetic and observation. The misfits of  $t_{\text{growth}}$  and  $t_{\text{decay}}$  help mitigate outlier effects and identify models with incorrect growth and decay times easily (Extended Data Fig. 7). They are an order of magnitude higher than the first term in equation (4) norm and thus, are down weighted by a factor of 10.

### Two-stage inner core growth

The conventional inner core growth model assumes that the inner core began to crystallize when molten iron cooled below the melting temperature at Earth's centre, followed by a steady growth stage that can be approximated as<sup>34</sup>  $R_{\text{ic}}(t) = R_{\text{ICB}}(t/\tau_{\text{ic}})^{0.4}$ , where  $R_{\text{ic}}$  is the inner core radius at time  $t$ ,  $R_{\text{ICB}}$  is the present inner core radius and  $\tau_{\text{ic}}$  is the inner core age when assuming the inner core would nucleate immediately after the liquid outer core cooled below its melting point<sup>34</sup>. However, this model neglects the energy barrier to the formation of the first stable crystal.

In general, a liquid must cool below the liquidus temperature (that is, supercooling) to overcome a nucleation barrier in forming the first stable crystal<sup>42</sup>. For example, water droplets must supercool to temperatures below  $-10$  °C before ice nucleates where dust is ubiquitous

# Article

or even to  $-37.5^{\circ}\text{C}$  in deep convective clouds<sup>43</sup>. Accounting for this phenomenon, a recent study<sup>30</sup> proposed the “inner core nucleation paradox” such that the inner core requires a supercooling of approximately 1,000 K below the melting temperature of the iron alloy to nucleate the first stable iron crystal based on classical nucleation theory<sup>42</sup>, which cannot be reconciled with a slow core cooling rate of approximately 100 K Gyr<sup>-1</sup> estimated from energy and entropy balance of a core with high thermal conductivity<sup>34</sup>. A subsequent study confirmed the paradox with atomic-scale simulations and pointed out that the paradox cannot be resolved with the presence of light elements during the nucleation process<sup>31</sup>. The plausible solution to the paradox must lower the nucleation energy barrier such that it only requires supercooling of at most 200 K below the melting temperature of iron alloy to form the first iron crystal<sup>30</sup>. After surpassing the nucleation barrier, the inner core initially crystallized very rapidly until supercooling at the ICB was close to zero. Then, the inner core transferred to a steady growth regime<sup>30</sup>. In this scenario, the inner core experienced a two-stage growth: a rapid initial growth stage on the timescale of thousands of years followed by a steady growth stage<sup>30</sup>, resulting in a younger inner core age than those estimated from the conventional growth model<sup>34,44,45</sup>.

Sumita et al.<sup>46</sup> showed that no significant residual melt exists in the inner core in a simple growth model because the compaction rate is faster than the solidification rate. However, the initial stage of fast growth in a two-stage growth scenario would have less complete compaction. Lasbleis et al.<sup>33</sup> revisited the model of Sumita et al.<sup>46</sup>. Without considering other thermal or compositional effects, they showed that delayed nucleation leads to an initially highly porous innermost inner core. We used a python package, mushdynamics (<https://github.com/MarineLasbleis/mushdynamics>), developed by Lasbleis et al.<sup>33</sup>, to model the compaction of the inner core as a two-phase flow system. We explored the time evolution of inner core porosity in two scenarios: classical inner core growth and growth with delayed nucleation. For the classical growth scenario, the inner core grew as<sup>34</sup>  $R(t) = R_{\text{ICB}}(t/\tau_{\text{ic}})^{0.4}$ , where  $R_{\text{ICB}}$  is the present inner core radius and  $\tau_{\text{ic}}$  is the inner core age. For the scenario with delayed nucleation, the inner core growth is in two stages: (1) an initial stage of rapid growth and (2) a second stage with slow growth similar to the classical scenario (Extended Data Fig. 8). We explored three cases for this scenario: delayed nucleation with first crystal occurrence at times of  $0.07 \tau_{\text{ic}}$ ,  $0.12 \tau_{\text{ic}}$  and  $0.18 \tau_{\text{ic}}$ , where  $\tau_{\text{ic}}$  is the presumed inner core age in the classical growth model. We set the initial porosity to 0.4 and the compaction length to  $0.1 R_{\text{ICB}}$  in all the simulations. The inner core porosity in the classical growth scenario is close to zero, aside from a thin mushy layer near the ICB (Extended Data Fig. 9). Like the classical growth scenario, the simulations with late crystallization exhibit a mushy layer on the top of the ICB; however, significant porosity initially exists inside the inner core in addition to the thin mushy layer (Extended Data Fig. 9). The trapped melt is likely to undergo freezing later in time as the inner core cools.

## Data availability

Requests for International Monitoring System array data can be completed online at <https://www.ctbto.org/specials/vdec/>. Data for ASAR and WRA can be downloaded from Incorporated Research Institutions for Seismology (IRIS; [www.iris.edu](http://www.iris.edu)) with network code AU. Data for ILAR, NVAR, PDAR and TXAR are available from IRIS with the network code IM; requests for YKA data can be submitted online at

<https://earthquakescanada.nrcan.gc.ca/fdsnws/>. The seismic data for XHDR can be downloaded from IRIS with network code XH, and the seismic data of YDWG and YDWS are available from IRIS with the network code YD in 2013–2014. The Global Centroid Moment Tensor earthquake catalogue is available at <https://www.globalcmt.org/CMTsearch.html>. Source data are provided with this paper.

## Code availability

The seismic array processing code used in this study is available online at <https://zenodo.org/record/6784342>. The numerical code for the inner core compaction model is available online at <https://github.com/MarineLasbleis/mushdynamics>. The numerical code for the phonon simulation is available online at <https://github.com/nmancinelli/psphonon>. All figures were generated using pygmt (<https://www.pygmt.org/latest/>).

35. Ekström, G., Nettles, M. & Dziewoński, A. M. The global CMT project 2004–2010: centroid-moment tensors for 13,017 earthquakes. *Phys. Earth Planet. Inter.* **200–201**, 1–9 (2012).
36. Margerin, L., Campillo, M. & Van Tiggelen, B. Monte Carlo simulation of multiple scattering of elastic waves. *J. Geophys. Res. Solid Earth* **105**, 7873–7892 (2000).
37. Mancinelli, N. & Shearer, P. Scattered energy from a rough core–mantle boundary modeled by a Monte Carlo seismic particle method: application to PKKP precursors. *Geophys. Res. Lett.* **43**, 7963–7972 (2016).
38. Takeuchi, N. et al. Determination of intrinsic attenuation in the oceanic lithosphere–asthenosphere system. *Science* **358**, 1593–1596 (2017).
39. Wang, W. & Shearer, P. M. Using direct and coda wave envelopes to resolve the scattering and intrinsic attenuation structure of Southern California. *J. Geophys. Res. Solid Earth* **122**, 7236–7251 (2017).
40. Weaver, R. L. Diffusivity of ultrasound in polycrystals. *J. Mech. Phys. Solids* **38**, 55–86 (1990).
41. Hedlin, M. A. & Shearer, P. M. An analysis of large-scale variations in small-scale mantle heterogeneity using Global Seismographic Network recordings of precursors to PKP. *J. Geophys. Res. Solid Earth* **105**, 13655–13673 (2000).
42. Kelton, K. & Greer, A. L. *Nucleation in Condensed Matter: Applications in Materials and Biology* (Elsevier, 2010).
43. Rosenfeld, D. & Woodley, W. L. Deep convective clouds with sustained supercooled liquid water down to  $-37.5^{\circ}\text{C}$ . *Nature* **405**, 440–442 (2000).
44. Konópková, Z., McWilliams, R. S., Gómez-Pérez, N. & Goncharov, A. F. Direct measurement of thermal conductivity in solid iron at planetary core conditions. *Nature* **534**, 99–101 (2016).
45. Ohta, K., Kuwayama, Y., Hirose, K., Shimizu, K. & Ohishi, Y. Experimental determination of the electrical resistivity of iron at Earth’s core conditions. *Nature* **534**, 95–98 (2016).
46. Sumita, I., Yoshida, S., Kumazawa, M. & Hamano, Y. A model for sedimentary compaction of a viscous medium and its application to inner-core growth. *Geophys. J. Int.* **124**, 502–524 (1996).

**Acknowledgements** We thank N. Mancinelli for sharing the phonon code and providing helpful modelling suggestions. We thank J. Vidale for helpful comments. This work was funded by the National Science Foundation (EAR-1722542). This work is approved for public release under LA-UR-22-28862.

**Author contributions** G.P. developed the array processing package gPar, analysed most array data, performed heterogeneity modelling and analysed inner core geodynamic evolution. K.D.K. supervised and acquired funding for the project and provided advice on data processing. S.-M.W. helped analyse array data. W.W. helped in the phonon scattering modelling. M.L. helped in the inner core compaction modelling. G.E. helped in funding acquisition and provided advice on data processing. All the authors contributed to the interpretation of the observations and in the preparation of the manuscript.

**Competing interests** The authors declare no competing interests.

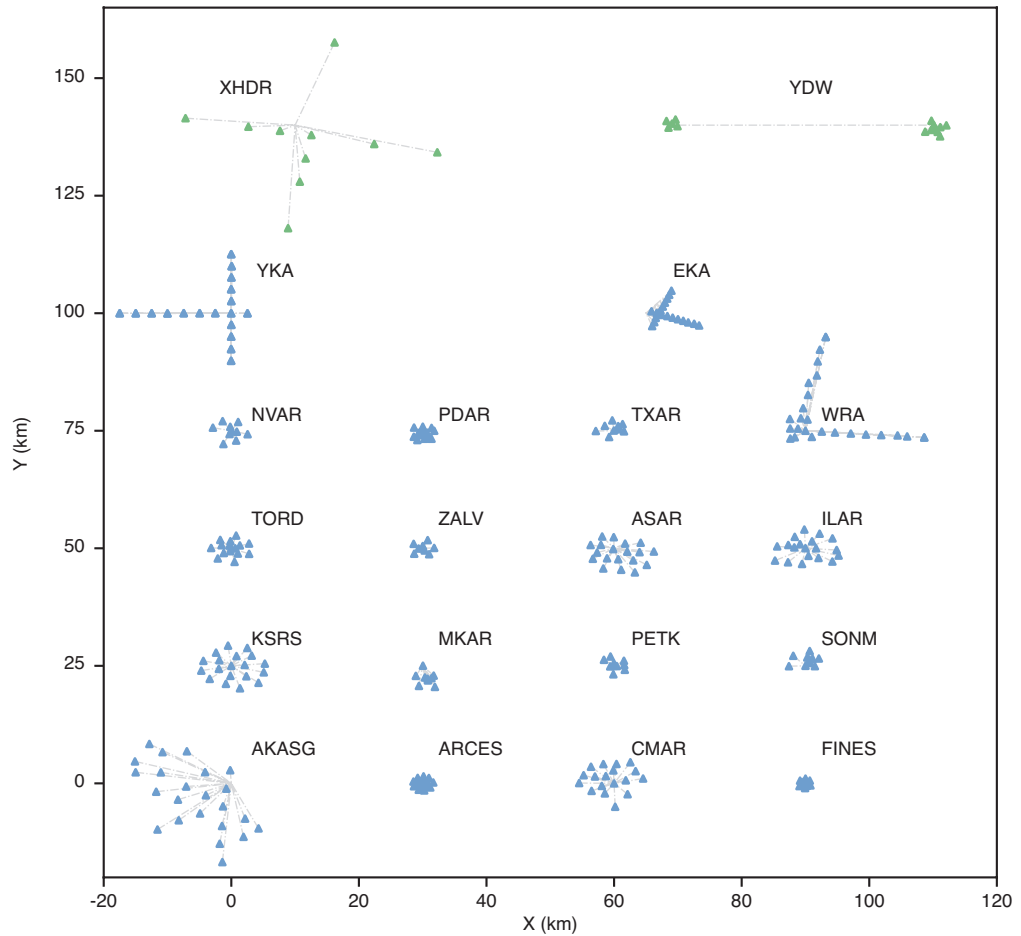
## Additional information

**Supplementary information** The online version contains supplementary material available at <https://doi.org/10.1038/s41586-023-06213-2>.

**Correspondence and requests for materials** should be addressed to Guanning Pang.

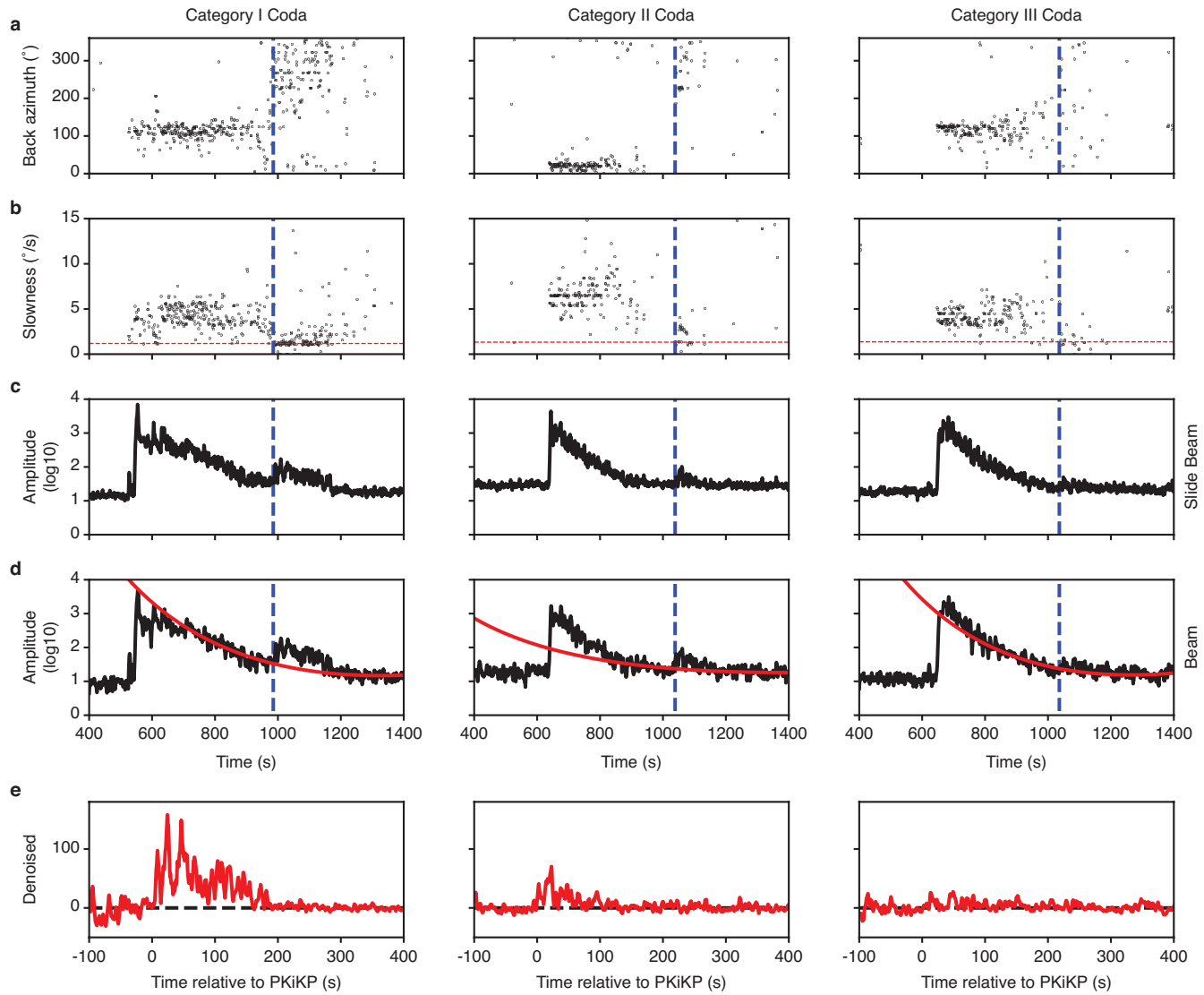
**Peer review information** *Nature* thanks Sebastian Rost and the other, anonymous, reviewer(s) for their contribution to the peer review of this work. Peer reviewer reports are available.

**Reprints and permissions information** is available at <http://www.nature.com/reprints>.



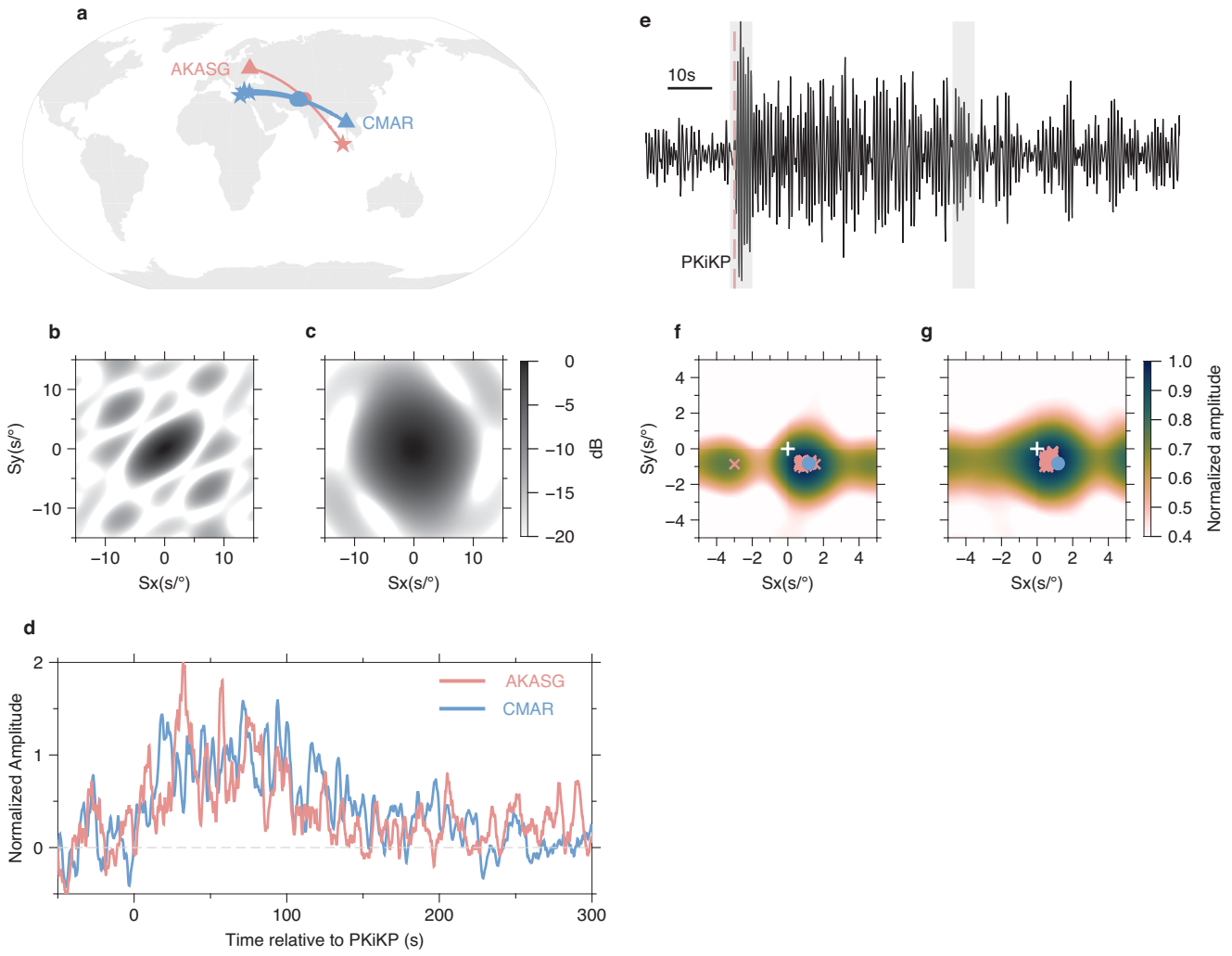
**Extended Data Fig. 1 | Array geometries and station codes.** The triangles (blue for IMS arrays and green for Antarctica networks) are individual array elements and the dashed grey lines link the elements to the array reference points.

# Article



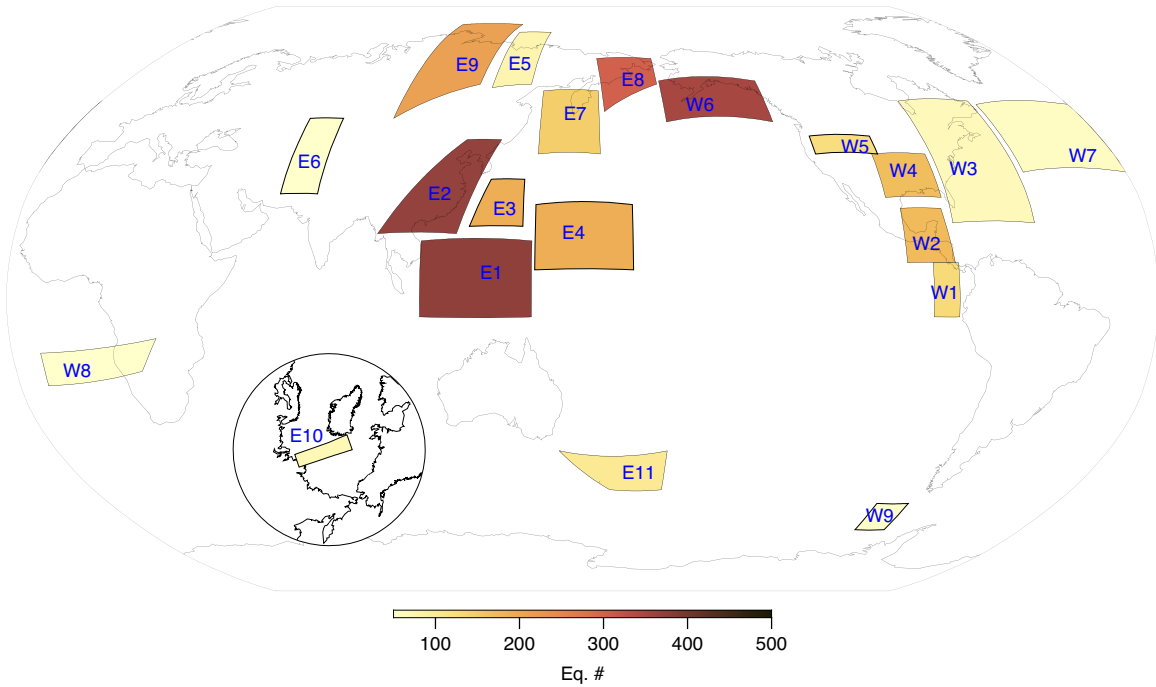
**Extended Data Fig. 2 | Example ICS observations in categories 1–3.** All three earthquakes were recorded in Chiang Mai, Thailand (CMAR) and had similar magnitudes ( $M_w \sim 6.3$ ). The blue-dashed lines mark the predicted  $PKiKP$  arrival time and the red dashed lines mark the theoretical  $PKiKP$  slowness. Rows **a** through **c** (back azimuth, slowness, and beam amplitude) show the results from

the sliding window slowness analysis, presented as a function of time relative to earthquake origin time. Row **d** shows envelopes of delay-and-sum beams formed at the theoretical  $PKiKP$  slowness. The red line is the best fitting curve to the background energy using the quasi-analytical coda decay model (Eq. (1)). Row **e** shows the denoised  $PKiKP$  envelopes as a function of time relative to  $PKiKP$ .

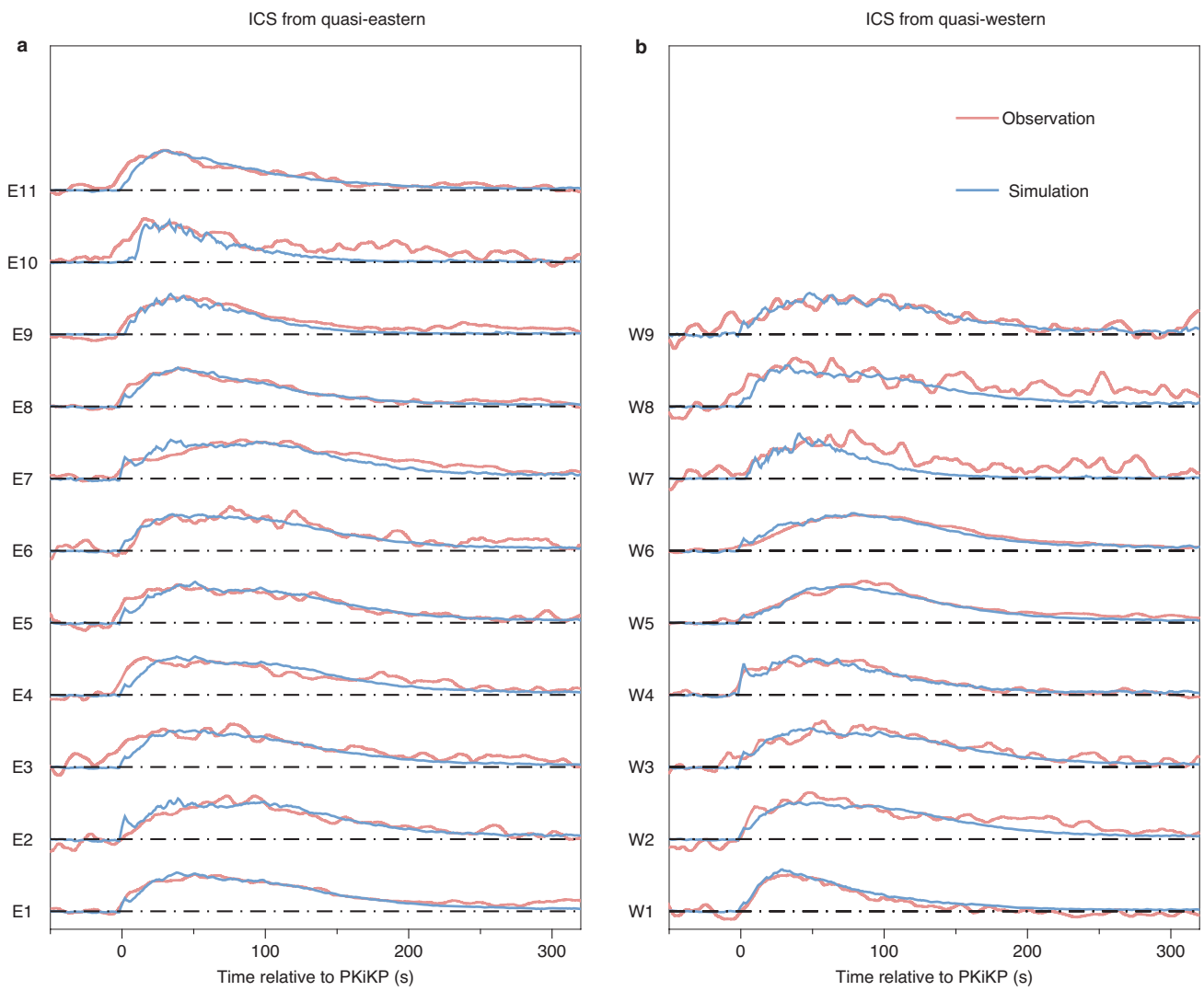


**Extended Data Fig. 3 | Overlapping PKiKP coda observations.** **a**, Locations of arrays AKASG (red triangle) and CMAR (blue triangle). The red star is a Category 1 earthquake recorded at AKASG and the blue stars are three Category 2 earthquakes recorded at CMAR. The solid lines are the ray paths from earthquakes to arrays and the dots are the corresponding bounce points on the ICB. These different earthquake-array combinations sample the same inner core region but different crust and mantle structure. Array response functions at 1 Hz with a slowness of 0 s/ $^{\circ}$  are shown for **b**, AKASG and **c**, CMAR. **d**, Single (red) and stacked (blue) denoised PKiKP envelopes from AKASG and CMAR, respectively. **e**, Example delay-and-sum beam at the YKA seismic array in Canada. The earthquake ( $M_w$  6.1, 2013/04/21 03:22:16 UTC, 29.93°N, 138.89.62°E,

422 km depth, USGS-NEIC) occurred near Japan about 71°. Grey windows mark the signals used in **f** and **g**. **f**, Slowness vector analysis of the direct PKiKP phase (first grey window on **e**). Blue dots mark the theoretical slowness from AK135. White crosses indicate vertical incidence. Pink crosses represent bootstrap solutions determined by repeating the slowness analysis for 50 randomly resampled sets of array elements. **g**, Similar to **f** but for a time window deep in the coda (second grey window on **e**). Note that the coda energy has a lower ray parameter than the direct PKiKP wave but with a similar back azimuth, implying that it is arriving from great circle heterogeneity deep within the inner core beneath the PKiKP bounce point.

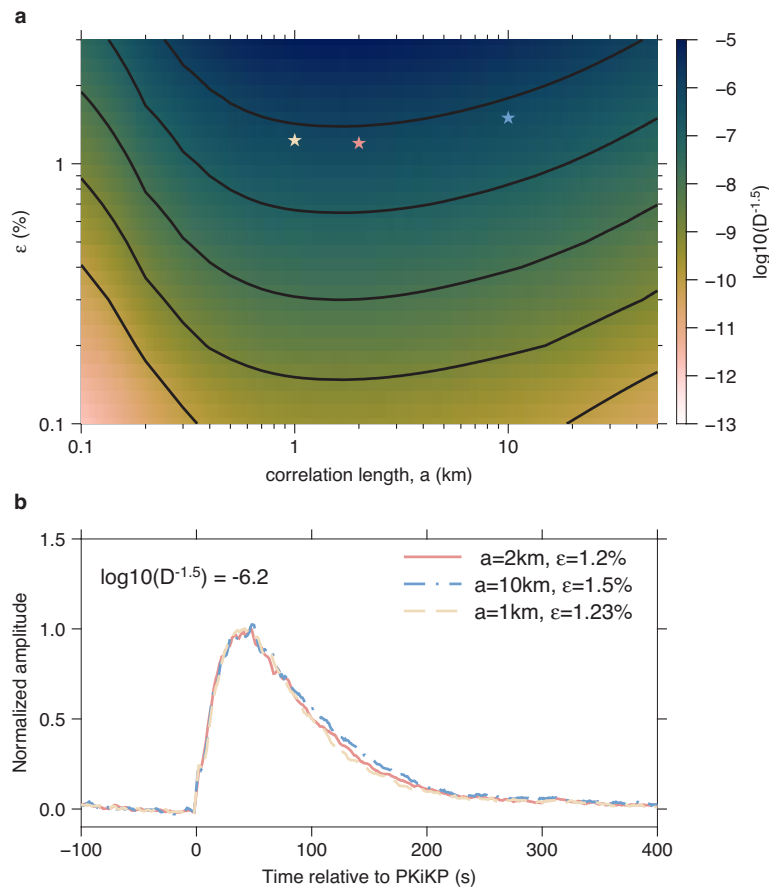


**Extended Data Fig. 4 | Geographic regions sampled in this study.** Names of regions located in the quasi-eastern hemisphere (longitude > 0) start with E. Names of regions in the quasi-western hemisphere (longitude < 0) start with W. The colour is the number of earthquakes that sampled the region.



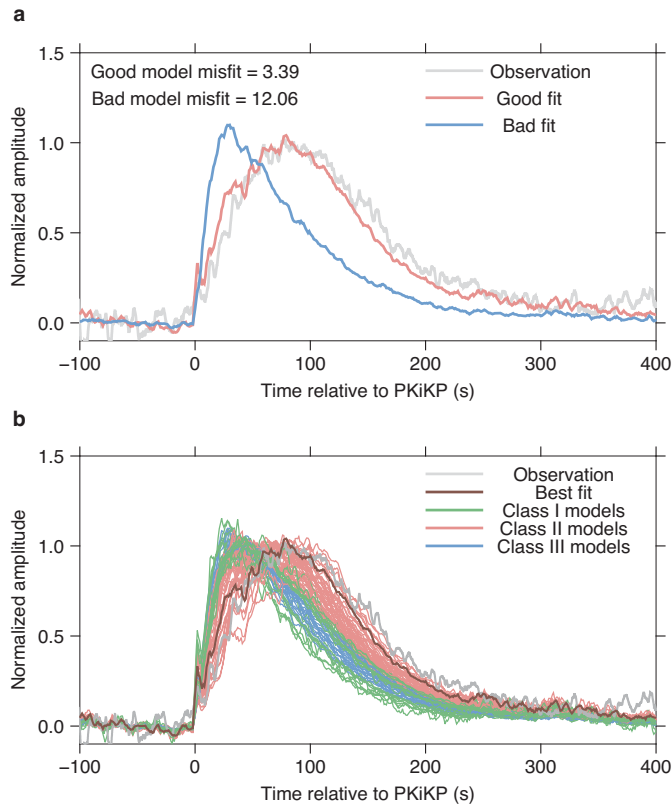
**Extended Data Fig. 5 | Observations and predictions of inner core scattered (ICS) energy.** The red lines are ICS envelope stacks sampling different inner core geographic regions (shown in Extended Data Fig. 4) observed at various

arrays. The blue lines are the corresponding best-fitting simulations from the multiple scattering phonon approach.



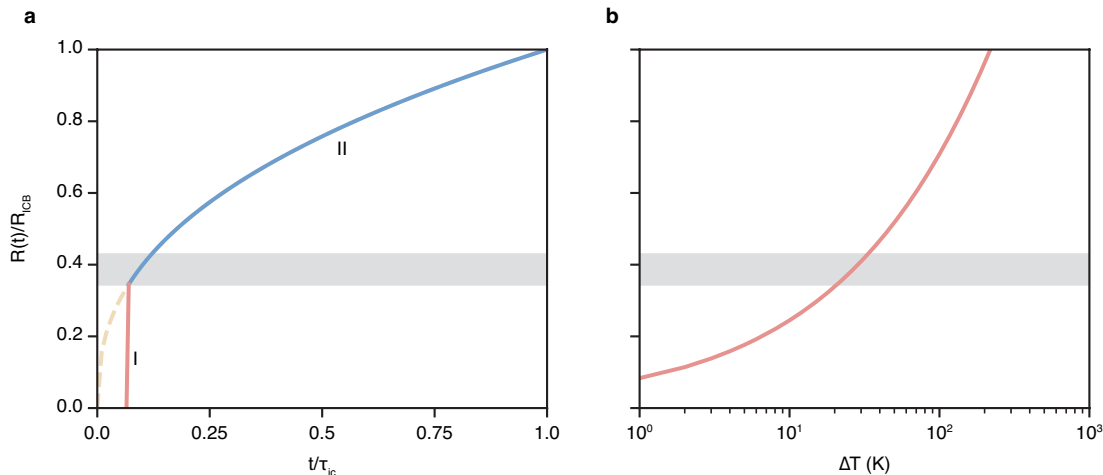
**Extended Data Fig. 6 | Trade-off between  $a$  and  $\varepsilon$ .** **a**, Backscattered energy ( $D^{-1.5}$ ) as a function of correlation length ( $a$ ) and root-mean-square velocity perturbation ( $\varepsilon$ ). Stars mark the  $(a, \varepsilon)$  pairs used in generating synthetic

envelopes shown in **b**. **b**, Synthetic envelopes from scattering models with the same diffusivity  $D$  but different  $(a, \varepsilon)$  pairs marked as stars in **a**.



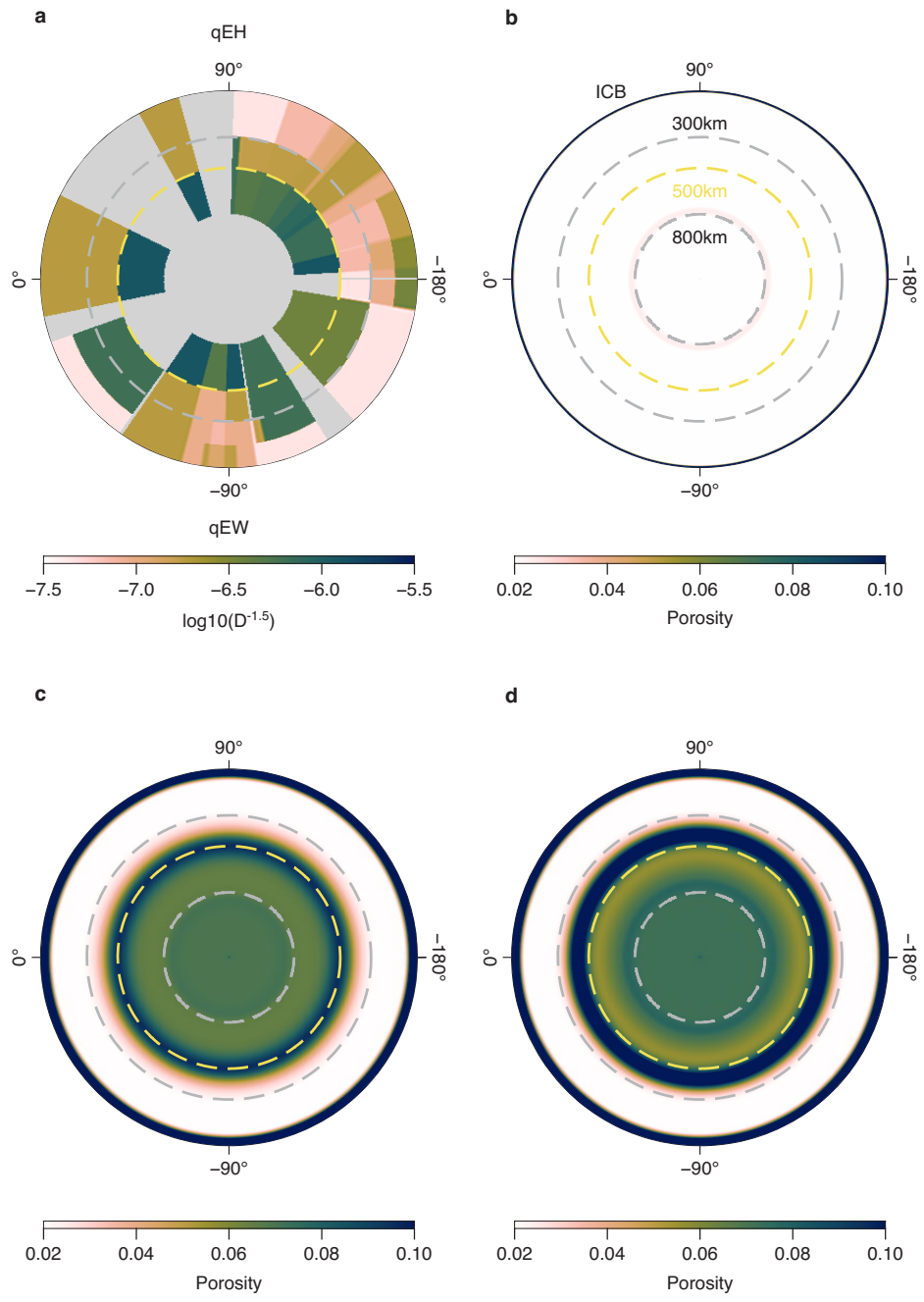
**Extended Data Fig. 7 | Phonon models and model fitting algorithm.**

**a**, A demonstration of the model fit using the algorithm in Eq. 4. The grey line is the observed ICS envelope. The red line is the best-fitting model prediction, and the blue line is a model prediction mismatching the observation by a factor of 4. **b**, All inner core heterogeneity models in this study. Green lines are the Class 1 models with uniform diffusivities. Red lines are the Class 2 models with stronger scattering strength in deep inner core. Blue lines are Class 3 models with weaker scattering with depth. The grey line is the same observation as in **a**. The brown line is the best-fit model.



**Extended Data Fig. 8 | Inner core two-stage growth model.** **a**, Inner core delayed nucleation and two-stage growth model. The inner core growth is in two steps: I. initial rapid growth stage (red segment); and II. Steady growth stage (blue). The right end of the x-axis is the present time. The left end, i.e., 0, is the moment when the centre of the primordial outer core cooled below its melting point. The y-axis is the normalized inner core radius at time  $t$ .  $R_{ICB}$  is the present inner core radius. The radius at the end of step I is a function of the

supercooling temperature, which is shown in **b**. **b**, The initial inner core radius at the end of the early rapid growth step (step I) as a function of the supercooling temperature at historical Earth centre, modified from Huguet *et al.*<sup>30</sup>. The grey zone denotes the historical inner core radius at the end of Step I in the porosity evolution with delayed nucleation at  $0.07\text{--}0.12\tau_{ic}$ , where  $\tau_{ic}$  is the presumed inner core age in the conventional growth model (dashed line in a).



**Extended Data Fig. 9 | Scattering strength and porosity along the radius of the inner core in the present day.** **a**, Global average scattering variation along the inner core radius. Inner core porosity structure based on three growth models: **b**, conventional inner core growth<sup>34</sup>; **c**, inner core nucleation delayed

to  $0.12\tau_{ic}$ , and **d**, inner core nucleation delayed to  $0.18\tau_{ic}$ . Yellow lines indicate 500 km below ICB, where the scattering strength increases globally.

# Article

**Extended Data Table 1 | Arrays in this study**

NET	NAME	LAT (°)	LON (°)	IMS	Elements	Aperture	Category	Category	Category		
							CODE	#	(km)	I (#)	II (#)
IM	AKASG	50.7012	29.2242	PS45	24	27.6	18	18	142		
IM	ARCES	69.5349	25.5058	PS8	26	3.1	27	7	117		
AU	ASAR	-23.6582	133.9305	PS3	19	10.1	2	19	125		
IM	CMAR	18.4205	98.9588	PS41	18	10.1	23	40	154		
IM	EKA	55.3339	-3.19229	AS104	21	8.7	8	3	133		
IM	FINES	61.4436	26.0771	PS17	16	2.0	13	1	161		
IM	ILAR	64.7714	-146.8861	PS49	19	10.2	56	85	205		
IM	KSRS	37.4766	127.894	PS31	19	10.1	16	16	106		
IM	MKAR	46.7937	82.2906	PS23	9	4.9	0	3	179		
IM	NVAR	38.4296	-118.3036	AS113	11	5.6	31	64	212		
IM	PDAR	42.7704	-109.5666	PS48	13	3.6	11	36	241		
IM	PETK	53.1082	157.6988	PS36	10	3.9	5	13	359		
IM	SONM	47.8347	106.395	PS25	10	5.0	8	8	174		
IM	TORD	13.1477	1.6947	PS26	16	6.1	1	3	50		
IM	TXAR	29.331	-103.674	PS46	9	4.4	5	37	265		
AU	WRA	-19.9469	134.3624	PS2	24	26.4	12	28	134		
CN	YKA	62.4932	-114.6053	PS9	18	22.7	59	105	416		
IM	ZALV	53.9481	84.8188	PS33	9	3.6	11	9	126		
YD	YDWG*	-84.593	-161.8949	nan	5	1.5	0	1	6		
YD	YDWS*	-84.4736	-157.7398	nan	9	3.4	6	4	11		
XH	XHDR	-78.9461	180.0	nan	11	40.0	8	11	109		

The columns LAT and LON give the array reference point. The aperture of the array is calculated from the maximum distance between a sensor pair in the array. YDWG and YDWS together compose the Antarctic array YDW (Extended Data Fig. 1).